ELSEVIER

Journal of Fluids and Structures 19 (2004) 1103–1115

JOURNAL OF FLUIDS AND STRUCTURES

www.elsevier.nl/locate/jnlabr/yjfls

Experimental flow study over a blunt-nosed axisymmetric body at incidence

D.K. Pantelatos, D.S. Mathioulakis*

School of Mechanical Engineering/Fluids Section, National Technical University of Athens, 9 Heroon Polytechniou Ave., 15710 Zografos Athens, Greece

Received 21 July 2003; accepted 20 July 2004
Available online 18 october 2004

Abstract

The flowfield over a blunt-nosed cylinder was examined experimentally at a low subsonic speed for $Re = 1.88 \times 10^5$ and angles of attack up to 40°. Velocity measurements were carried out (employing a seven-hole Pitot tube) as well as wall static pressure and wall shear-stress measurements. Surface flow visualization was applied using liquid crystals and a mixture of oil–TiO_2. For all the examined cases no flow asymmetries were found. For high angles of attack (20° and above) a separation "bubble" appears at the leeside of the nose area (streamwise flow separation). The basic feature of the circumferential pressure distribution at the after body area for these angles of attack is a plateau close to the suction peak and a fast recovery next to it. One streamwise vortex on each side of the symmetry plane is formed as well as a separation bubble about 90° far from this plane, where the cross-flow primary separation line is located. Each cross-flow primary separation line starts at the leeside nose area and moves towards the windward side along the cylindrical after body. The space between the two primary separation lines close to the wall is characterized by high flow fluctuations on the leeside, compared to the low fluctuations of the windward side.

1. Introduction

The flow over an inclined axisymmetric body presents interesting features due to the variety of both longitudinal and circumferential pressure gradients. From a practical point of view, the study of such flows is related to the motion control of bodies like aircraft, submarines and missiles. The complex flow patterns of this application constitute a great challenge for a numerical analyst if a flow prediction is necessary for the proper design and control of such bodies, aiming at enhancing their manoeuvrability, especially at high angles of attack.

Increasing the angle of attack, both streamwise and cross-flow adverse pressure gradients cause flow separation. A common flow feature between sharp- and blunt-nosed inclined cylinders is the formation of two streamwise vortices on the leeside of the body. With respect to the symmetry plane, defined by the free-stream velocity and the longitudinal axis of the body, these vortices are symmetrically positioned for the blunt- nosed cylinders, independently of the angle of attack (Hoang et al., 1997), until the onset of shedding. However, for the sharp-nosed cylinders this symmetry breaks down beyond a certain angle, associated with the appearance of a significant side force (Ericson and Reding, 1986). The formation of a leeside vortex is the result of an adverse circumferential pressure gradient which causes a so-called

*Corresponding author. Tel.: +30 210 77 21 028; fax: +30 210 77 21 057.
E-mail address: mathew@fluid.mech.ntua.gr (D.S. Mathioulakis).

0889-9746/$ - see front matter © 2004 Elsevier Ltd. All rights reserved.
doi:10.1016/j.jfluidstructs.2004.07.004

"open" or "free vortex layer" separation (Maskel, 1955; Legendre, 1956; Wang, 1972). In addition to this, for the blunt-nosed cylinders a "bubble" type separation occurs at the leeside nose area, upstream of the previous one due to a positive longitudinal pressure gradient (Hsieh and Wang, 1996; Hoang et al., 1997). However, for high angles of attack and low Reynolds numbers (Re) of the order of 10^4 (based on the cylindrical after body diameter) these two types of separation are converted to the closed one, since there is no gap between the two separation regions. Keeping the same angle of attack and increasing Re to about one order of magnitude higher, both the bubble and open separations appear again (Hoang et al., 1999). Apparently, Re is a very important parameter for this kind of 3-D flow fields, as well as the angle of attack and the free-stream turbulence level, since they influence the point of transition to turbulence and consequenly the separation location. In order to fix the transition point, many experimentalists trip the boundary layer at the nose area by attaching a wire to the model surface, so that flow separation is less sensitive to Re and thus its location is close to that of the full scale body (Chesnakas and Simpson, 1997).

Systematic experiments on ogive cylinders by Lamont (1982) have shown that, dependent on Re and angle of attack, cross-flow separation can be classified according to the following three types: laminar, transitional and turbulent. According to the transitional type, laminar separation is followed by turbulent reattachment, forming a short bubble close to the suction peak, while towards the leeside of the body turbulent separation takes place again. The critical Re corresponding to the boundary between the laminar and transitional type of separation was found to be of the order of 3×10^5 for ogive cylinders, independent of the angle of attack, whereas between the transitional and turbulent ones, this is an increasing function of the angle of attack (Lamont, 1982). Based on flow visualization, it has been shown (Keener, 1986) that all three types of flow separation can take place for a certain angle of attack at different parts of an axisymmetric body.

The flow picture close to the surface of axisymmetric bodies has been examined by many researchers through surface flow topology (Wang, 1972; Costis et al., 1989; Patel and Kim, 1994; Hsieh and Wang, 1996; Hoang et al., 1997), presenting the characteristics of the limiting streamlines, separation lines, singular points, like saddle points, nodes, foci, etc. (Tobak and Peak, 1982). Moreover, wall shear stresses on a prolate spheroid, based on LDV velocity profiles, have shown different characters of 3-D flow separation compared to the 2-D one (Chesnakas and Simpson, 1997), according to which a local minimum of wall shear stress does not coincide with flow reversal but it is rather located further downstream. This finding is in agreement with shear-stress measurements carried out by another group (Kreplin et al., 1982). More about this important issue of cross-flow separation are discussed in Wetzel et al. (1998).

The present study refers to the low subsonic flow over an axisymmetric body, the nose of which is part of a hemisphere, connected smoothly to a cylindrical after body. The majority of the published works on this topic have focused on transonic or low supersonic flows over similar bodies, excluding the low subsonic regime (Hoang et al., 1997). In order to obtain a good picture of this complex flow field, static pressure, wall shear stress and velocity measurements were performed, as well as surface flow visualization, at various angles of attack.

2. Experimental procedure

The flow about an axisymmetric body was studied at various angles of attack in the range 0–40°. The nose of the body was part of a sphere (in fact less than a hemisphere of radius 45 mm), joined smoothly to a cylindrical after body (base diameter $D = 127$ mm) within a distance of 165 mm from the body tip (see Fig. 1) through a circular arc. Therefore, the fineness ratio was $165/127 = 1.3$ and the bluntness ratio $2 \times 45/127 = 0.7$. The model, made of aluminium, with a total length of 500 mm was placed in the test-section (1800×1400 mm^2) of a closed circuit subsonic wind tunnel. Maximum wind tunnel blockage, defined, as the ratio of the projected frontal area of the model to the wind tunnel cross-sectional area was less than 4% for all the examined cases.

In order to record both the longitudinal and circumferential pressure distributions, pressure holes were drilled along a generator (their locations are shown in Table 1) as well as at the periphery of four cross-sections in the body nose area. These sections were named A, B, C, D at distances 31.4, 67.83, 104.25 and 165 mm, from the nose tip, respectively. The last section, D, coincided with the beginning of the cylindrical after body, and section A with the end of the spherical nose. Copper tubes of 0.8 mm inner diameter were inserted at the pressure holes inside the hollow aluminium model, connected via plastic tubes to a 48-port pressure scanivalve. In order to avoid long transients, the scanivalve was installed inside the model, reducing the distance between the measuring points and the pressure transducer. The analogue output of the scanivalve corresponded to the difference between the local static pressure from the free-stream static pressure, the latter measured by a Pitot-static tube. Since only 48 points could be measured by the scanivalve (a small number, if a good picture of the pressure distribution around the body is desired), an electric motor was installed at the trailing edge of the model, rotating the model about its long axis with an accuracy of one degree (Fig. 1). Therefore, pressure measurements were repeated by rotating the model with increments of 30°, until a full revolution

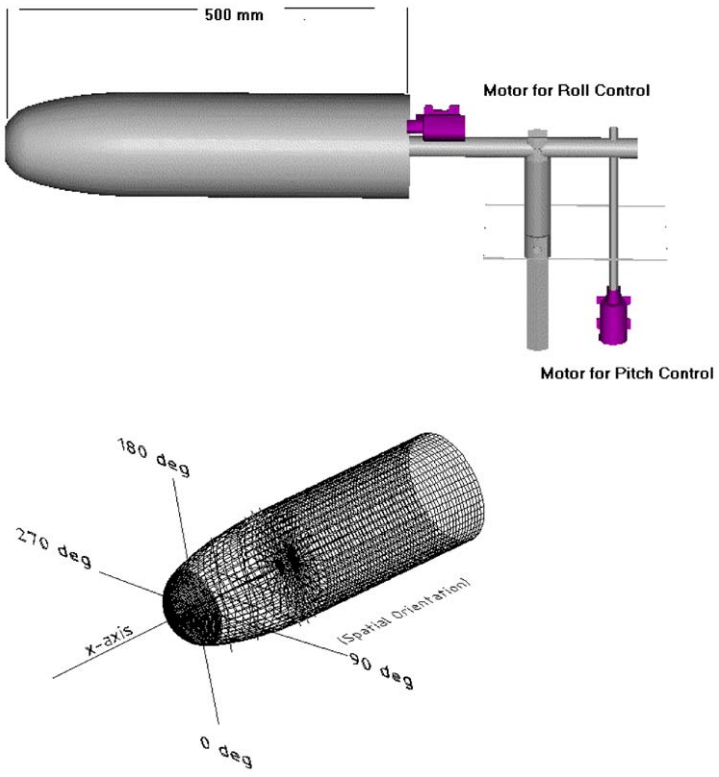

Fig. 1. Axisymmetric model and coordinate system.

Table 1
Locations of pressure taps along a generator (distance from nose tip in mm)

0	1	4	8	15	23	31	44	56	68	80	92	104	116	129
141	153	165	213	228	243	258	273	288	303	343	358	378	398	

was complete. Normally, 564 data-points were obtained during a full turn of the body. However, in the nose area a step of 5° was used in some cases in order to provide more details of the flow picture in this important region.

At sections A, B and C, only four pressure taps were positioned at diametrically opposite points, in order to record flow asymmetries, if any, and at the same time avoid a probable triggering of flow asymmetries due to the pressure holes themselves. As has been documented (Hoang et al., 1997), small protuberances in the nose area of a hemispherical cylinder can cause strong flow asymmetries. However, in section D, since this was located at the end of the nose, it was decided to open more pressure taps, due to the fact that surface irregularities in this region do not affect the flow. In the above-mentioned work it was found that the influence of mounting a small bead on the body surface is minimal when this is placed inside or downstream of the nose separation bubble. By rotating the body with a step of 30°, a detailed pressure distribution was obtained at this particular cross-section, due to many pressure taps distributed at its periphery.

The angle of attack α, defined as the angle between the free-stream velocity U and the longitudinal axis of the body, was adjusted either by rotating this axis at a certain angle (pitch angle) with respect to U (being horizontal) or by rotating the vertical sting of the wind-tunnel balance, upon which the model was mounted (yaw angle).

The velocity field was measured over the cylindrical after body, using a seven-hole Pitot tube (Aeroprobe Corp.). The diameter of this tube at the base of its conical tip was 3 mm, and it was moved via a stepper motor along a radial direction in a region of 5–32 mm ($0.25D$) far from the body, with its axis parallel to the body surface. The tube and its traversing mechanism were attached to the rotating body, so that the velocity vectors were measured along the

circumference of a given cross-section at various radial distances from the surface. More emphasis was given on the leeward side of the model, where the flow separates and reattaches, forming two coherent stream wise vortices. Errors associated with this kind of probe have been documented by Rediniotis et al. (1993), providing comparisons with LDV measurements, for the case of a spherical nose cylinder at an angle of attack.

In order to obtain more information about the flow characteristics close to the body wall, a DANTEC hot-film (55R47) was attached to it. The sensor surface covered an arc length of about 7° along the circumference of the after body and it was connected to a DANTEC constant temperature bridge (56C17CTA). The azimuthally variation of its output was recorded by rotating the body with 10° increments from 0° to 360°. This was repeated at 10 axial stations along the body at which the sensor was mounted. Since the output of this sensor was very sensitive to fluid temperature changes, hot-film measurements were initiated after the wind-tunnel temperature had reached a constant value. Since this temperature varied from one experimental run to another, a good effort was made to calibrate the sensor using the Preston tube technique. Because of the big wind tunnel temperatures variations (of the order of 25 °C, for the examined range of free-stream velocities during calibration), there was no formula found to safely relate the output voltage with the shear stress. Therefore, it was decided to use the sensor output in order to show the relative wall shear-stress magnitude distribution at each axial station, whereas its fluctuations provided a picture of the flow disturbances level close to the wall.

Finally, flow details, in a qualitative manner, were documented by surface flow visualization that was performed using liquid crystals as well as a mixture of oil–TiO_2. Liquid crystals (Hallcrest Ltd) were sprayed on the model surface, which previously was painted black. When the liquid crystals were exposed to the flow they were coloured according to the local shear stress. A characteristic example is the recirculation zones, the colour of which differs from the part of the surface where the flow is included. Besides liquid crystals, a mixture of oil–TiO_2 was used as well, covering the body surface with a thin film. Regions of low velocity or low shear, e.g. separation bubbles, are distinguished due to the higher mixture concentrations at these regions.

3. Results and discussion

The experiments were carried out at $\mathrm{Re} = 1.88 \times 10^5$ based on the after body diameter, and for angles of attack in the range 0–40°. Longitudinal pressure distributions (along various generators) as well as circumferential ones at various cross-sections were recorded. The x-axis of the used coordinate system was parallel to the longitudinal body axis, with $x = 0$ at the body tip. The angle φ(0–360°) along the circumferential direction had its origin ($\varphi = 0°$)($\varphi = 0°$) at the symmetry plane of the windward side of the body (Fig. 1). The pressure coefficient c_p is presented, defined as

$$c_p = \frac{p - p_\infty}{\rho U^2/2},$$

where p_∞ and U are the free-stream static pressure and velocity, respectively. The variation of the c_p time-mean values at any point did not exceed the range ± 0.04 based on repeatable measurements made at the same meridional and axial location, through different pressure taps, rotating the model about its longitudinal axis. The axial pressure distribution through 29 stations along four generators ($\varphi = 0°$, 90°, 180°, 270°) and four angles of attack $\alpha = 10°$, 20°, 30°, 40° are presented in Fig. 2. A common feature of these graphs is the strong axial pressure gradients in the curved nose area that in the afterbody becomes insignificant. As expected, on the windward symmetry plane ($\varphi = 0°$) pressure takes its maximum value close to the tip, due to the presence of the stagnation point and then it drops due to flow acceleration, levelling off at the after body. This final value of c_p depends on the angle of attack, being an increasing function of it. More specifically, these values varied between -0.1 at $\alpha = 10°$ to 0.4 at $\alpha = 40°$. Concerning the location of the stagnation point ($c_{p\max}$) on generator $\varphi = 0°$ this moves downstream with increasing angle of attack, from $x = 0.99$ mm at $\alpha = 10°$ to $x = 14.97$ mm at $\alpha = 40°$. On the suction side symmetry plane ($\varphi = 180°$), pressure takes a minimum value in the nose area and then it recovers to a value close to the free-stream static pressure, independently of the angle of attack. The suction peak ($c_{p\min}$) increased, in absolute value, when the angle of attack increased. Namely, for $\alpha = 10°$, $c_{p\min} = -0.55$; for $\alpha = 20°$, $c_{p\min} = -0.7$; for $\alpha = 30°$, $c_{p\min} = -1.1$; and for $\alpha = 40°$, $c_{p\min} = -1.2$. Moreover, for $\alpha \geqslant 20°$ and $\varphi = 180°$there is a pressure plateau downstream of the suction peak at the end of the spherical part of the nose. This pressure plateau is associated with a separation bubble that is a characteristic feature of the flow over hemisphere cylinders. This separation bubble has been documented by various researchers, like Hsieh and Wang (1996), Hoang et al. (1997), Barberis (1986), who found that its shape depends on the angle of attack, Reynolds number and Mach number. In the present work, the pressure plateau along $\varphi = 180°$ moves upstream with increasing α. The existence of this bubble was also documented through flow visualization. Using liquid crystals (Fig. 3(a) and 3(b)), the bubble for $\alpha = 40°$ is clearly distinguished from the rest of the model surface due to its different (green) colour. Fig. 3(a) is a side

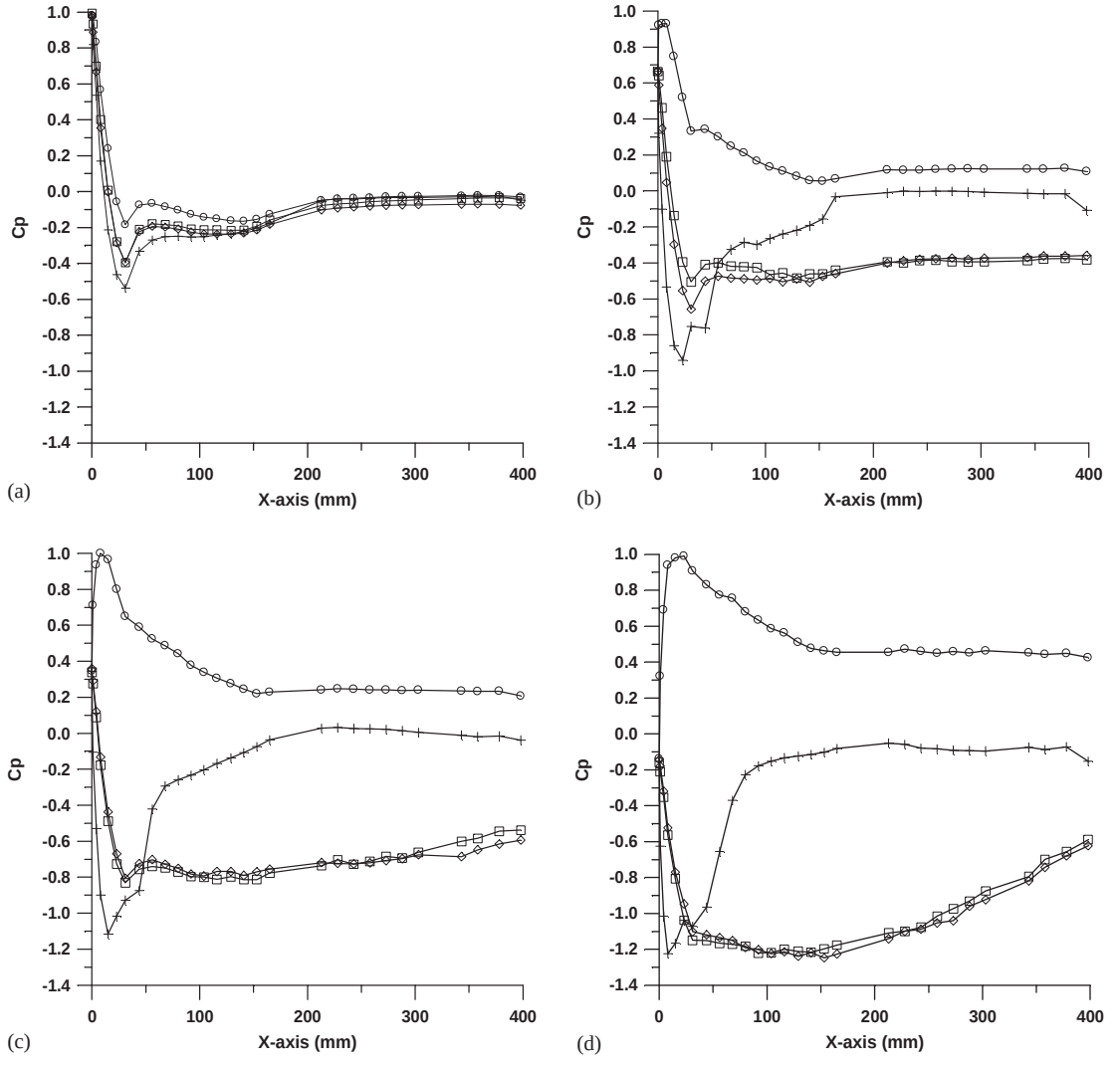

Fig. 2. Axial pressure distributions for four angles of attack: (a) $\alpha = 10^\circ$, (b) 20°, (c) 30°, (d) 40°, along four generators. $\circ$, $\varphi = 0$; $+$, $\varphi = 180^\circ$; $\square$, $\varphi = 90^\circ$; $\diamond$, $\varphi = 270^\circ$.

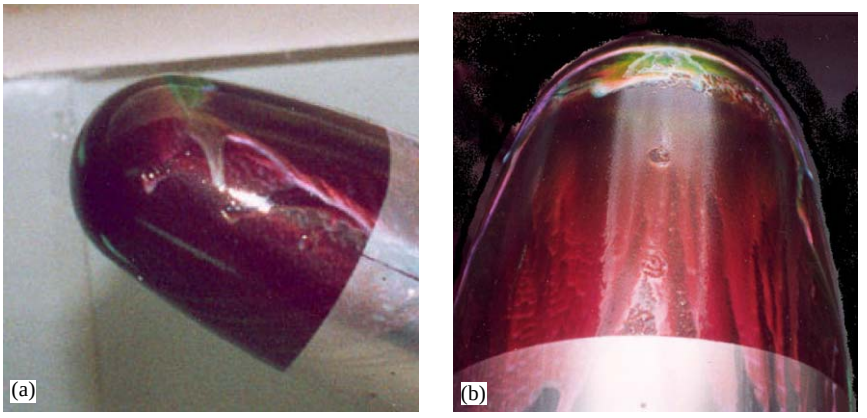

Fig. 3. Flow visualization using liquid crystals, $\alpha = 40^\circ$. Nose separation bubble (green colored): (a) side view, (b) top view.

view ($\varphi = 0-180^\circ$) and Fig. 3(b) a top view ($\varphi = 90$–270°) of the model. A similar picture was obtained using the oil–TiO_2 technique (Fig. 4(a)). Besides, the separation bubble in the nose area, the primary separation line along the body axis is clearly shown in Fig. 4, as well as the limiting streamlines of the windward side that converge towards the separation line.

The pressure distributions along $\varphi = 90^\circ$ and 270° were essentially the same within the experimental uncertainty, indicating that the flow is symmetric. Only for $\alpha = 20^\circ$ is there some asymmetry in the nose area, which however is not present further downstream, indicating that this is not systematic. The pressure is reduced with a high rate from the nose tip till section A and then it recovers ($\alpha \leqslant 30^\circ$) or it drops with a much smaller rate ($\alpha = 40^\circ$). In the after body region there are no pressure changes for $\alpha = 10^\circ$ and 20° along these generators. However, for higher angles of attack ($\alpha = 30^\circ$ and 40°) the pressure progressively increases along x, since the flow in the circumferential direction separates earlier (smaller φ) with increasing x. Hoang et al. (1999) found that cross-flow over a hemisphere cylinder for $\alpha = 20^\circ$ and $Re = 2.9 \times 10^5$ separates between $\varphi = 130^\circ$ close to the nose and $\varphi = 100^\circ$ at the after body. Similar observations have been reported by Wetzel et al. (1998) and Constantinescu et al. (2002) for blunt-nosed cylinders. This type of 3-D separations is an open type (Wang, 1972) since fluid particles reach both sides of the separation line, originating from the same area. For one order of magnitude lower Re (2.7×10^4) it was found by Hoang et al. (1997) that, for the hemisphere cylinder and $\alpha > 20^\circ$, flow separation was of the closed type, since the nose separation bubble was connected with the downstream separated flow without any gap between them.

A detailed picture of cross-flow is given in Fig. 5, presenting static pressure versus azimuth angle φ, for four angles of attack, $\varphi = 10^\circ$, 20°, 30° and 40°. Based on this figure, three basic shapes of pressure distribution are recognized.

(a) Pressure is decreasing from $\varphi = 0^\circ$ to 180° where a suction peak is located (Fig. 5(a)). This type of distribution is found only in the nose area and $x < 31.4$ mm for $\alpha > 10^\circ$. When α increases this region shrinks, namely for $\alpha = 20^\circ$ this extends from the nose tip to $x = 22.67$ mm, for $\alpha = 30^\circ$ to $x = 14.97$ mm, and for $\alpha = 40^\circ$ to $x = 8.36$ mm.

(b) Downstream of this region but still in the nose area, a suction peak appears accompanied by a relatively small recovery (Fig. 5(a)). This suction peak moves towards the windward side of the model with increasing x. For instance, for $\alpha = 40^\circ$, this moves from $\varphi = 130^\circ$ to 115° in the region $x = 14.97$–31.4 mm.

(c) Further downstream ($x > 67.83$ mm for $\alpha = 40^\circ$) till the end of the body, the pressure exhibits a suction peak (at $\varphi = 80^\circ$ for $\alpha = 40^\circ$); next, a small recovery ending to a plateau (between $\varphi = 100^\circ$ and 120° for $\alpha = 40^\circ$); then, a faster recovery; and finally a second plateau close to the leeside symmetry plane (Fig. 5(b)). For smaller angles of attack, pressure distributions are similar with the one for $\alpha = 40^\circ$, with the only difference that the suction peaks are displaced to higher azimuth angles. The pressure plateau in the circumferential direction is an indication of cross-flow separation, namely one close to $\varphi = 100^\circ$ and the other towards the leeside symmetry plane. Due to the complex character of the 3-D separation (Simpson, 1996) more parameters have to be examined to reveal its details. Therefore, these regions were further investigated by employing a seven-hole Pitot tube, a wall shear-stress sensor, and flow visualization. According to Fig. 4, high concentrations of oil–TiO_2 appear close to $\varphi = 100^\circ$ for $\alpha = 40^\circ$, apparently as a result of low wall shear stresses and low fluid velocities, both of which characterize a separation region. Therefore, this is additional proof that there is a separation bubble close to $\varphi = 100^\circ$. Next to this region and for a range of $\Delta\varphi \approx 20^\circ$, the model surface is clean, indicating flow reattachment, and towards the leeside symmetry plane the surface is again covered by oil–TiO_2 apparently due to cross-flow separation. The pressure plateau close to the suction peak and the subsequent fast recovery is characteristic of the transitional type of separation, based on the 2-D flow about cylinders (Lamont, 1982). In the laminar separation case, next to the suction peak, there is a pressure dip, whereas in the turbulent case, pressure varies

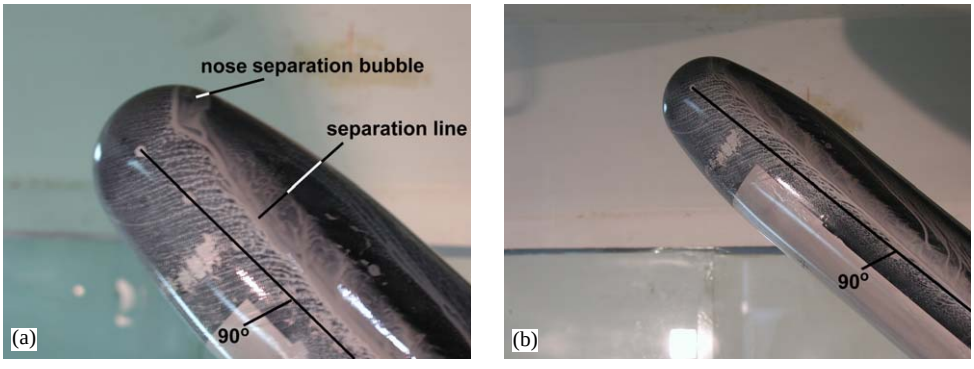

Fig. 4. Flow visualization using oil–TiO_2, $\alpha = 40^\circ$ showing the nose separation bubble and the primary separation line.

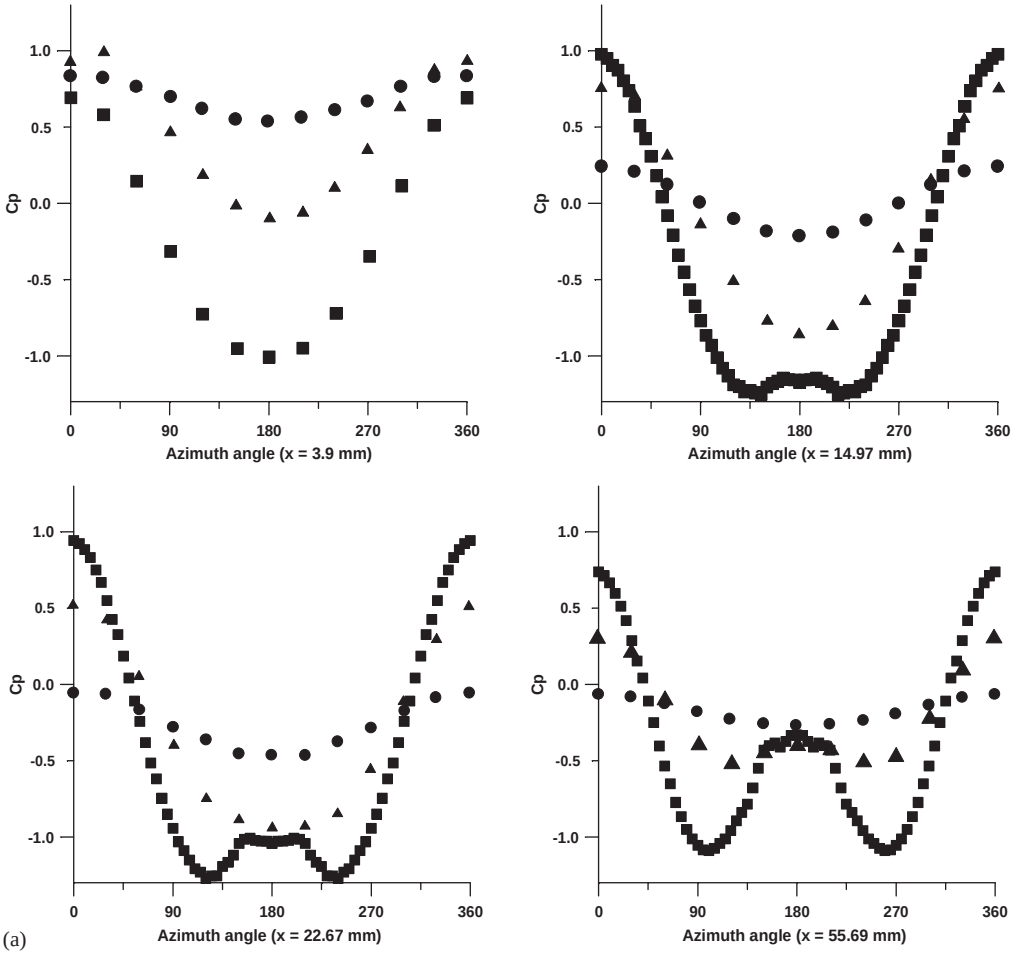

Fig. 5. Circumferential pressure distribution (a) for $\alpha = 10^\circ$ (○), 20° (▲), 40° (■) at $x = 3.9$, 14.97, 22.67 and 55.69 mm and (b) at $x = 165$ mm for $\alpha = 10^\circ$, 20°, 30°, 40°.

more or less as in inviscid flow, up to the separation point (Lamont, 1982). The influence of Re for $\alpha = 40^\circ$ was examined for the range $(0.94–1.9) \times 10^5$, measuring the pressure distribution at section D (where the after body starts). For this range of Re, the azimuthal pressure distribution is essentially the same up to $\varphi = 120^\circ$, beyond which this is dependent on Re (Fig. 6(a)). Increasing Re, the pressure dip (next to the suction peak) progressively decreases and finally it disappears (for $\mathrm{Re} = 1.65 \times 10^5$), forming a plateau next to the suction peak. In order to further increase Re (artificially), a trip wire at the mid length of the nose was mounted. The diameter of the wire was 0.5 mm, according to a formula given by Rae and Pope (1984). The influence of the wire is clearly shown in the pressure distribution (Fig. 6b), looking like the turbulent flow case (without any plateau or dip close to the suction peak).

The velocity vectors (three velocity components) at the cylindrical after body were measured by employing a seven-hole Pitot tube. Representative pictures of the cross-flow for $\alpha = 40^\circ$ at three axial stations are displayed in Fig. 7. The closest to the surface measurement was 5 mm from it, the distance between two neighbouring vectors in the radial direction was 3 mm (equal to the probe diameter) and in the circumferential direction 5°. It is clearly shown that the cross-flow close to the wall starts decelerating at a certain azimuthal angle dependent on x ($\varphi = 125^\circ$ at $x = 165$ mm, $\varphi = 120^\circ$ at $x = 226\ 288$ mm) and finally turns negative. The recorded flow upstream of this area behaves like an inviscid one, namely the velocity component parallel to the surface is decreasing in the radial direction, being apparently outside of the boundary layer region. The negative flow region is part of a cross-flow vortex, the size of which increases downstream and lifts off the body surface. At $x = 165$ mm the vortex has not been shaped yet, but at $x = 226$ mm it is well defined, with its center at $\varphi = 150^\circ$ and 8 mm from the surface. Further downstream ($x = 288$ mm), the vortex is

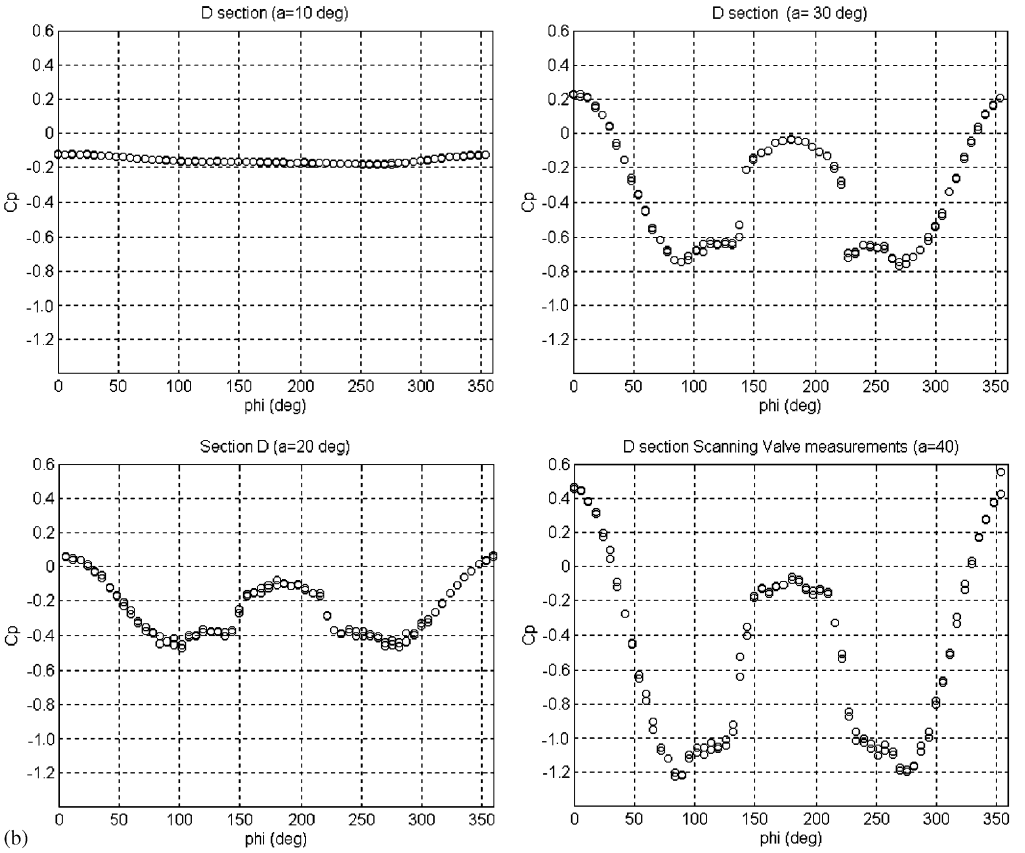

Fig. 5. (*Continued*)

larger, and its centre has moved to 11 mm away from the surface at $\varphi = 160^\circ$. Due to the symmetry of the flow, the same picture holds on each side of the symmetry plane. Velocity measurements close to $\varphi = 100^\circ$ did not reveal the existence of a separation bubble, due to the presence of the Pitot tube which in such recirculation regions of small extent may destroy them. In order to examine the influence of the Pitot tube on the flow due to its proximity to the wall, pressure measurements were made on section $x = 288$ mm for various distances of the tube from the body. Fig. 8 shows the pressure distribution for two distances from the surface, namely 3 and 18 mm (for the latter distance the influence of the tube was minimal). It is obvious that the pressure distribution is mainly affected in the region from $\varphi = 40^\circ$ to 120°, in which pressure takes smaller values when the tube is close to the surface, and the first plateau essentially disappears. However, although it seems that its influence is smaller at the vortex region (at least with regard to wall pressure distribution), systematic comparisons with LDV (Hoang et al., 1999) showed that the velocity is underpredicted by the seven-hole Pitot tube when velocity gradients are high, like in a vortex. It is also noteworthy that there is a local pressure minimum at $\varphi = 160^\circ$, above which the vortex center is located. The same observations have been made by others (Chesnakas and Simpson, 1997; Hoang et al., 1997) calling this minimum the "footprint" of the vortex.

Fig. 9 presents details of the velocity field 5 mm far from the surface between $\varphi = 90^\circ$and 180° for $\alpha = 40^\circ$ at station $x = 288$ mm, including the velocity magnitude (*vel*), the cross-flow velocity component (w) which is parallel to the surface and normal to the x-axis, and the flow angle, the tangent of which is the ratio of w to the axial component of the velocity. According to Fig. 9 the velocity magnitude takes its minimum at $\varphi = 135^\circ$ where w also changes its sign. Cross-flow separation takes place where the velocity component normal to the separation line becomes zero. However, it should be stressed that the exact location of flow separation can be identified by nonintrusive techniques, taking measurements very close to the body surface. According to Wetzel et al. (1998), LDV measurements on a prolate spheroid showed that the change of the sign of w took place within a region of about 30° in the circumferentail direction, for a radial distance of 5 mm from the surface (when the local diameter of the body was 229 mm). Maximum

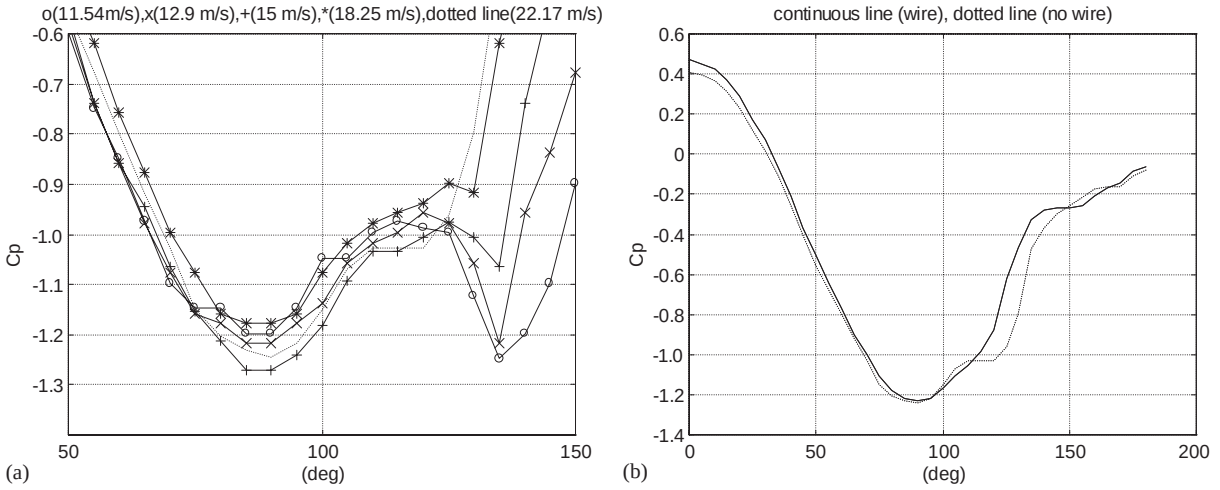

Fig. 6. Pressure distribution at (a) $x = 165$ mm versus Re. (b) $x = 165$ mm with and without trip wire.

values of both *vel* and *w* were close to the free-stream velocity (Fig. 9). In the region $\varphi < 130^\circ$ the flow angle was about 65° (25 degrees higher than the angle of attack), and in the vortex area it dropped to 35° tending to zero at the leeside symmetry plane. In a flow study over a prolate spheroid (Chesnakas and Simpson, 1997), the flow angle in the attached region for $\alpha = 10^\circ$ was 9 degrees higher than α, and for $\alpha = 20^\circ$, 15 degrees higher. The flow angles in the whole examined region (up to 32 mm from the surface) are shown in Fig. 10, represented by vectors parallel to the body surface. In the attached region, the angle distribution in the radial direction is essentially uniform. Approaching the point where *w* changes sign and downstream of this, a maximum of flow angle appears, as well as points of zero flow angle which are displaced far from the surface with increasing φ, following the detached cross-flow shear layer. At the leeward symmetry plane ($\varphi = 180^\circ$) the flow angle is minimized due to the flow symmetry.

More information was added to the flow picture by wall shear-stress measurements, carried out at 10 cross-sections from $x = 44$ to 385 mm. Representative data are shown in Fig. 11 for $\alpha = 40^\circ$. In these graphs the output time mean voltage of the hot-film sensor, namely the relative time mean wall shear stress magnitude distribution is shown as a function of the azimuthal angle in the interval 0°–180°. In order to present all distributions in one figure, an arbitrary value was added to each one of them. Excluding the area close to the nose tip, the shape of these distributions is characterized by two minima, which correspond to the two cross-flow separation regions (Wetzel et al., 1998). The first minimum of the graphs of Fig. 11 appears at azimuthal angles which are progressively reduced from $\varphi = 140^\circ$ at $x = 44$ mm to $\varphi = 90^\circ$ at $x = 385$ mm. It should be recalled that the pressure suction peak in the same region occurs earlier (between $\varphi = 80^\circ$ and 100°), since downstream of this angle there is a pressure recovery followed by flow separation. Therefore, based on this evidence, the primary separation line for $\alpha = 40^\circ$ lies between $\varphi = 140^\circ$ and $\varphi = 90^\circ$. Flow visualization (Fig. 4b) shows that this line goes through $\varphi < 90^\circ$ towards the end of the body, which means that the separation line defined by the hot-film output minima is located at higher φ compared to that defined by the oil–TiO_2 mixture. A similar behaviour was documented by Wetzel et al. (1998), providing as probable explanation the action of gravity upon the oil–TiO_2 mixture. Fig. 12 shows the location of the hot film minimum versus *x* for three angles of attack, namely $\alpha = 20^\circ$, 30° and 40°. The basic trend is that when α and/or *x* increase, cross-flow separation takes place earlier (smaller φ).

Concerning the fluctuations of the hot-film signal (r.m.s. values), these increase at a fast rate, upstream of the shear stress minimum, within a range of $\delta\varphi = 10^\circ$ to 30° and they remain high till the symmetry plane (Fig. 13). In Fig. 13, like in Fig. 11, each r.m.s. versus φ distribution has been displaced along the vertical axis by an arbitrary value. It is characteristic that along the windward attachment line ($\varphi = 0$), r.m.s. values are low and of the same level. However, approaching the primary separation line in the circumferential direction, rms starts increasing a little upstream of this line in the nose area and further upstream in the after body area. Considering that the cross-flow separation is of the transitional type, the flow is laminar in the windward side, the increased fluctuations of which are due to the separation region which becomes stronger streamwise. In contrast, for fully turbulent flow over an axisymmetric body, Chesnakas

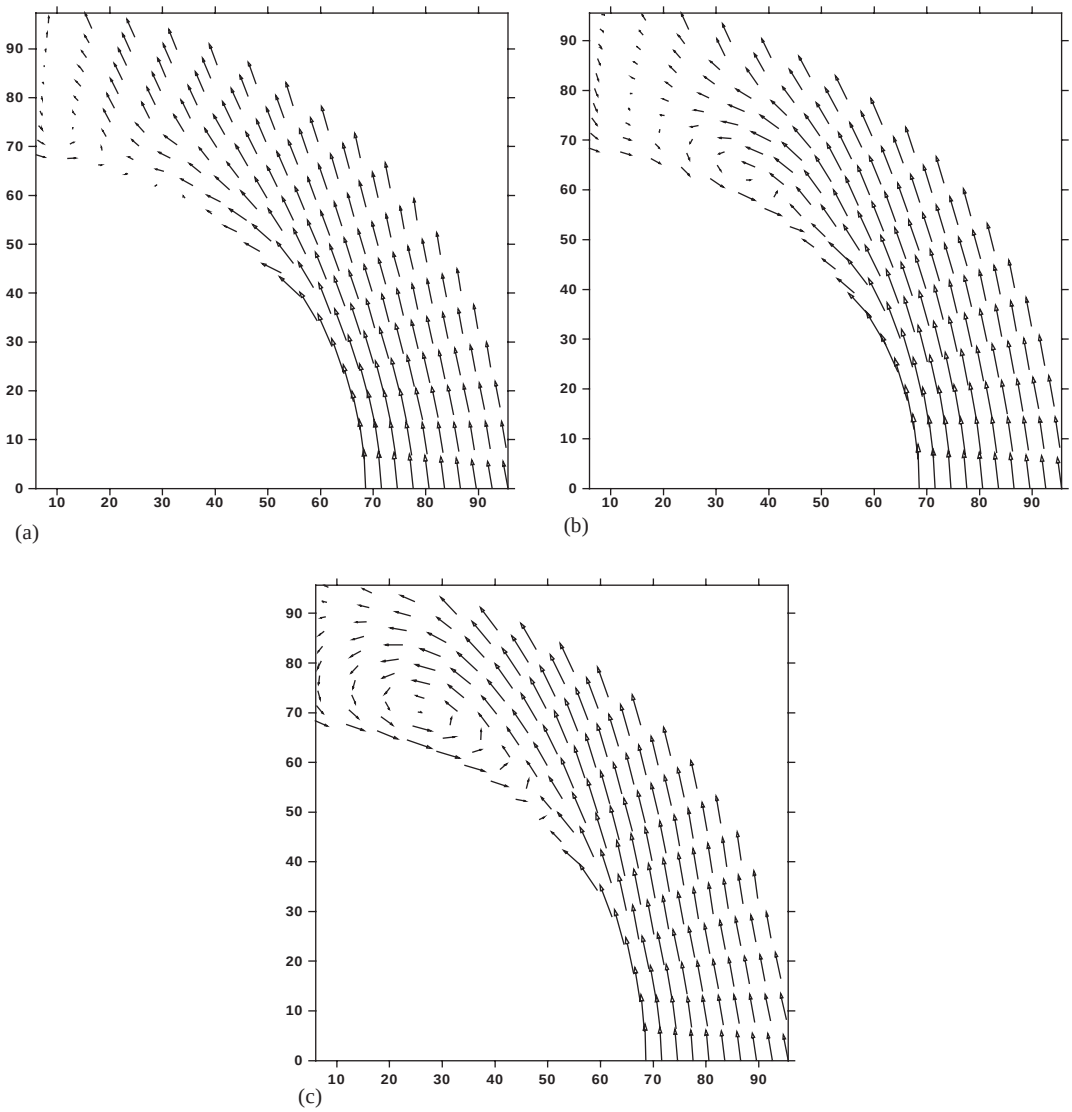

Fig. 7. Cross-flow velocity vectors, $\alpha = 40^{\circ}$: (a) $x = 165$ mm, (b) $x = 226$ mm, (c) $x = 288$ mm.

and Simpson (1997) found that, downstream of the separation line and for a small distance from this, the flow fluctuations were extremely low.

4. Conclusions

The flowfield over an inclined blunt-nosed axisymmetric body was experimentally studied at a low subsonic speed for $\mathrm{Re} = 1.88 \times 10^5$ and four angles of attack, namely $\varphi = 10^{\circ}$, 20°, 30° and 40°. In order to adequately explore this complex flow case, various techniques were employed: wall static pressure and wall shear-stress measurements, velocity measurements using a seven-hole Pitot tube and surface flow visualization using liquid crystals and a mixture of oil–TiO_2.

For all the examined cases, no flow asymmetries were detected, in agreement with the existing literature relevant to blunt-nosed cylinders. Due to strong longitudinal pressure gradients when $\alpha \geq 20^{\circ}$, a separation "bubble" appears at the lee side nose area, moving upstream with increasing α. In the cylindrical after body, flow separation takes place both

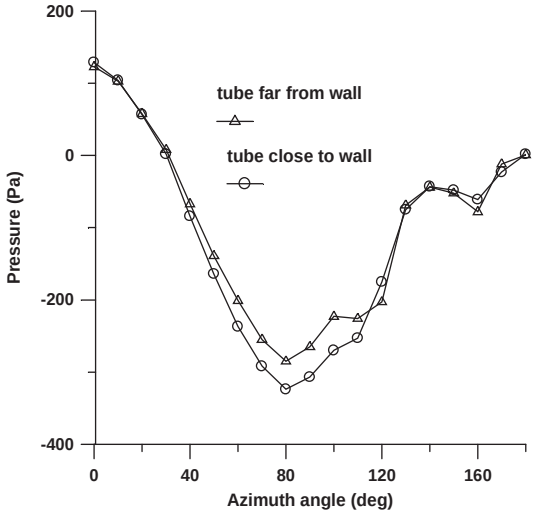

Fig. 8. Seven–hole Pitot tube close to the wall. Pressure distribution for $x = 288\,\text{mm}$, $\alpha = 40^\circ$.

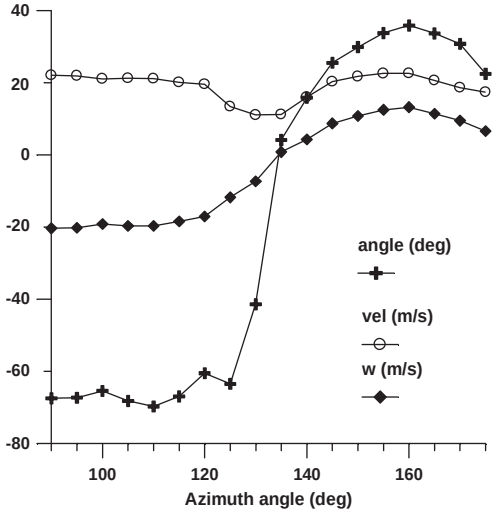

Fig. 9. Velocity magnitude (vel), crossflow velocity component (w), and flow angle $\alpha = 40^\circ$, $x = 288\,\text{mm}$.

close to $\varphi = 100^\circ$ forming a separation bubble, as well as close to the symmetry plane where two coherent vortices appear, one on each side of this plane. The characteristic feature of the circumferential pressure distribution at the after body area is a plateau next to the suction peak and then a fast recovery ending at another plateau at the symmetry plane. This cross-flow separation is of the transitional type according to 2-D flow about cylinders. Surface flow visualization and shear-stress measurements indicate that the primary separation line and a separation bubble attached to it move from the leeward side of the nose area towards $\varphi = 90^\circ$ at the cylindrical after body. Increasing α, this line is displaced to the windward side, showing that flow separation takes place there earlier. Flow fluctuations close to the wall are high between the two primary separation lines on the leeside of the body. However, dependent on the strength of the separated flow, these fluctuations appear also a certain distance upstream of the separation lines towards the windward side.

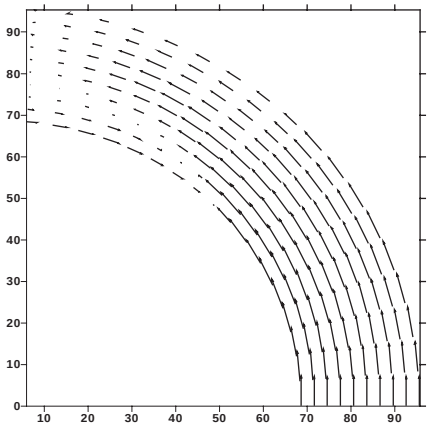

Fig. 10. Flow angle distribution, $\alpha = 40^\circ$, $x = 288$ mm.

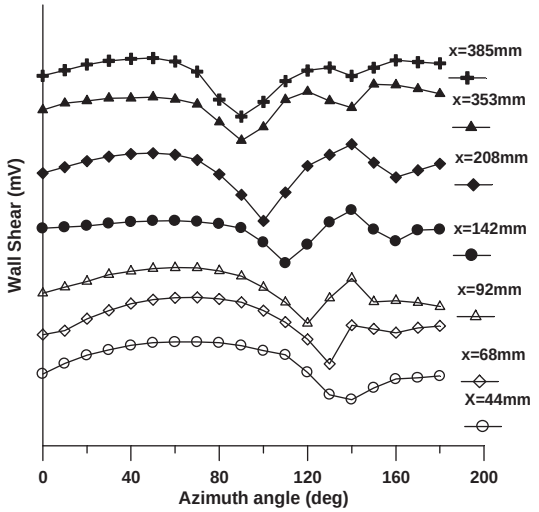

Fig. 11. Wall shear-stress relative magnitude, $\alpha = 40^\circ$.

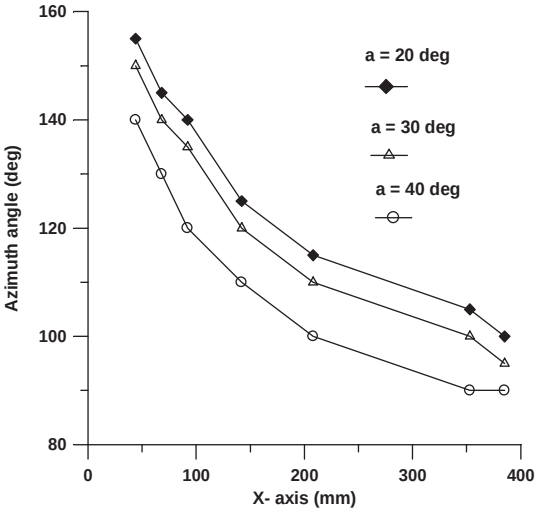

Fig. 12. Hot-film output minimum locations $\alpha = 20^\circ$, 30° and 40°.

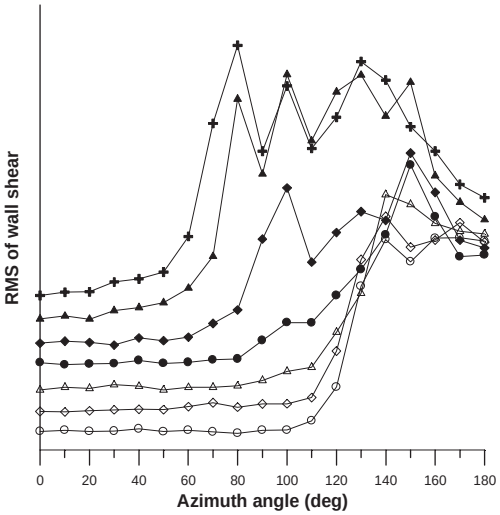

Fig. 13. RMS of hot-film output in the circumferential direction (for symbols, see Fig. 11.).

References

Barberis, D., 1986. Boundary layer computation on arbitrary obstacles with direct and inverse methods. La Recherche Aerospatiale, 1–27.

Chesnakas, C.J., Simpson, R.L., 1997. Detailed investigation of the three-dimensional separation about a 6:1 prolate spheroid. AIAA Journal 35, 990–999.

Constantinescu, G.S., Pasinato, H., Wang, Y.-Q., Squires, K.D., 2002. Numerical Investigation of flow past a prolate spheroid. AIAA Paper 2002-0588, presented at the Aerospace Sciences Meeting, Reno Nevada, 14–18 January 2002.

Costis, C.E., Hoang, N.T., Telionis, D.P., 1989. Laminar separating flow over a prolate spheroid. Journal of Aircraft 26, 810–816.

Ericson, L.E., Reding, J.P., 1986. Asymmetric vortex shedding from bodies of revolution. In: Hemsch, M.J., Nielsen, N.J. (Eds.)., Tactical Missile aerodynamics Progress in Astronautics and Aeronautics, Vol. 104. AIAA, New York, pp. 243–296.

Hoang, N.T., Rediniotis, O.K., Telionis, D.P., 1997. Symmetric and asymmetric separation patterns over a hemisphere cylinder at low Reynolds numbers and high incidences. Journal of Fluids and Structures 11, 793–817.

Hoang, N.T., Rediniotis, O.K., Telionis, D.P., 1999. Hemisphere cylinder at incidence at intermediate to high Reynolds numbers. AIAA Journal 37, 1240–1250.

Hsieh, T., Wang, K.C., 1996. Three-dimensional separated flow structure over a cylinder with a hemispherical cap. Journal of Fluid Mechanics 324, 83–108.

Keener, E. R., 1986. Flow-separation patterns on symmetric forebodies. NASA Report TM86016.

Kreplin, H.P., Vollmers, H., Meier, H.U., 1982. Measurements of the wall shear stress on an inclined prolate spheroid. Zeitschrift fur Fluguwissenschaften und Weltraumforschung 6, 248–252.

Lamont, P.J., 1982. Pressures around an inclined ogive cylinder with laminar, transitional, or turbulent separation. AIAA Journal 20, 1492–1499.

Legendre, R., 1956. Separation de l'ecoulement laminaire tridimensionel. La Recherche Aeronautique 54, 3–8.

Maskel, E. C., 1955. Flow separation in three dimensions. Royal Aircraft Establishment, Rept. No. Aero 2565.

Patel, V.C., Kim, S.E., 1994. Topology of laminar flow on a spheroid at incidence. Computers Fluids 23, 939–953.

Rae, W.H., Pope, A., 1984. Low-speed wind tunnel testing, second ed. Wiley, New York, p. 453.

Rediniotis, D.K., Hoang, N.T., Telionis, D.P., 1993. The seven-hole probe: its application and use. In: Industrial Fluid Dynamics Experiments, FED-vol.152. ASME, New York, pp. 21–26.

Simpson, R.L., 1996. Aspects of turbulent boundary-layer separation Prog. Aerospace Sci. 32, 457–521.

Tobak, M., Peak, D.J., 1982. Topology of three-dimensional separated flows. Annual Review of Fluid Mechanics 14, 61–85.

Wang, K.C., 1972. Separation patterns of boundary layers over an inclined body of revolution. AIAA Journal 10, 1044–1050.

Wetzel, T.G., Simpson, R.L., Chesnakas, C.J., 1998. Measurement of three-dimensional crossflow separation. AIAA Journal 36, 557–564.